

Sum-Frequency and Second-Harmonic Generation from Plasmonic Nonlinear Nanoantennas

*Xiaoyan Y. Z. Xiong¹, Li Jun Jiang¹, Wei E. I. Sha¹,
Yat Hei Lo¹, and Weng Cho Chew^{1,2}*

¹Dept. of Electrical and Electronic Engineering
The University of Hong Kong, Hong Kong
E-mail: xyxiong@eee.hku.hk, jianglj@hku.hk, weisha@zju.edu.cn, yathei36@gmail.com

²Dept. of Electrical and Computer Engineering University of Illinois at Urbana-Champaign
Urbana, USA
E-mail: w-chew@uiuc.edu

Abstract

Plasmonic nanostructures that support surface plasmon (SP) resonance potentially provide a route for the development of nanoengineered nonlinear optical devices. In this work, second-order nonlinear light scattering – specifically, sum-frequency generation (SFG) and second-harmonic generation (SHG) – from plasmonic nanoantennas is modeled by the Boundary-Element Method (BEM). Far-field scattering patterns are compared with the results calculated by the Mie theory to validate the accuracy of the developed nonlinear solver. The sum-frequency generation from a multi-resonant nanoantenna (MR-NA) and the second-harmonic generation from a particle-in-cavity nanoantenna (PIC-NA) are analyzed by using the developed method. Enhancements of the scattering signals due to double-resonance of the multi-resonant nanoantenna and gap plasmonic mode of the particle-in-cavity nanoantenna are observed. Unidirectional nonlinear radiation for the particle-in-cavity nanoantenna is realized. Moreover, the emission direction of this radiation can be controlled by the location of the nanosphere. This work provides new theoretical tools and design guidelines for plasmonic nonlinear nanoantennas.

1. Introduction

Plasmonic nanoantennas made from nanostructured metals have attracted significant attention in nonlinear optics, due to their unique properties [1]. One such property is their ability to concentrate light in nanoscale volumes, and to subsequently boost the intensity of local fields near particle

surfaces due to surface plasmon resonance (SPR) [2]. The surface-plasmon-resonance-enhanced near fields allow weak nonlinear processes – which depend superlinearly on the local fields – to be significantly amplified, giving rise to a promising research area called nonlinear plasmonics. The second-order nonlinear processes, e.g., sum-frequency generation (SFG) and second-harmonic generation (SHG), are significantly dependent on the symmetry of both the material being used and the structure being studied [3]. They are forbidden in the bulk of centrosymmetric media under the electric dipole approximation. However, the breaking of inversion symmetry at surfaces results in surface nonlinear scattering [4, 5]. The combination of nonlinear surface sensitive and strong near-field enhancement associated with surface plasmon resonance provides a unique tool for ultra-sensitive shape characterization [6, 7], super-resolution imaging, sensing and microscopy [8, 10], on-chip optical-frequency conversion, switching and modulation [11], etc.

Efficient nonlinear scattering requires the presence of strong nonlinear polarization sources at the surface of nanostructures, as well as efficient scattering of the signal into the far field. Analogous to classical antennas, the objective of nonlinear nanoantenna design is the optimization and control of the spatial distribution of scattered light. Several strategies have been applied to enhance the scattered nonlinear signals, including engineering near-field-coupled nanoparticle clusters associated with Fano resonances [12, 13], enhancing the electric fields using nanogaps [14], etc. However, tailoring the radiation pattern of nonlinear nanoantennas has great challenges. First, nonlinear radiation exhibits complex

multi-polar interactions [15, 16]. Second, currently, few tools are available for efficient and rigorous analyses of surface nonlinear scattering processes in complex structures. The volume-discretization-based full-wave methods, e.g., the Finite-Difference Time-Domain (FDTD) and the Finite-Element Method (FEM), are inefficient and inaccurate for solving surface nonlinear problems. Third, the relationship among plasmon resonances, particle geometry, and associated local-field distributions is very complicated [17]. Physical principles and design rules for nonlinear nanoantennas have not yet been explored.

In this work, a numerical solution based on the Boundary-Element Method (BEM) is proposed for the second-order surface nonlinear scattering problems. The proposed method is efficient with a surface discretization, and it can directly employ experimentally tabulated material parameters. The developed solver was utilized to systematically analyze the sum-frequency generation from a multi-resonant nanoantenna (MR-NA), and second-harmonic generation from a novel particle-in-cavity nanoantenna (PIC-NA) with strong surface plasmon resonance.

The remainder of this article is organized as follows. In the next section, we describe the Boundary-Element Method used in our study. Section 3 contains the main results. We first validate the accuracy of the developed solver by comparing the far-field scattering patterns with Mie-theory results. The sum-frequency generation from multi-resonant nanoantenna and the second-harmonic generation from particle-in-cavity nanoantenna are then analyzed. Finally, in the last section, we summarize the main conclusions of our work.

2. Methods

The second-order surface nonlinear problem, under the *undepleted-pump approximation*, can be described by the following driven wave equation, with the nonlinear polarization of the medium as a source term [18]:

$$\nabla^2 \mathbf{E}^{(\nu)} + k^{(\nu)2} \mathbf{E}^{(\nu)} = -\frac{\nu^2}{\epsilon_0 c^2} \mathbf{P}^{(\nu)}, \quad (1)$$

where $k^{(\nu)}$ is the wave number at frequency ν , and $\mathbf{P}^{(\nu)}$ is the surface nonlinear polarization at frequency ν . This has the form, $\mathbf{P}^{(\nu)} = \epsilon_0 \chi^{(2)} : \mathbf{E}_1^{(\omega_1)} \mathbf{E}_2^{(\omega_2)}$ and $\nu = \omega_1 + \omega_2$ for sum-frequency generation. The second-harmonic generation process is a special case of sum-frequency generation with $\omega_1 = \omega_2$ and $\nu = 2\omega_1$. $\chi^{(2)}$ is the surface second-order nonlinear susceptibility tensor. $\mathbf{E}_1^{(\omega_1)}$ and $\mathbf{E}_2^{(\omega_2)}$ denote the fundamental fields at frequencies ω_1 and ω_2 , respectively. The symbol “:” is a tensor operator that functions as

$$P_i^{(\nu)} = \sum_{j,k} \chi_{ijk}^{(2)} E_{1j}^{(\omega_1)} E_{2k}^{(\omega_2)}.$$

Metals are centrosymmetric materials. The surface of metal nanoparticles has an isotropic symmetry with a mirror plane perpendicular to it. The surface susceptibility tensor has only three non-vanishing and independent elements:

$$\begin{aligned} \mathbf{P}^{(\nu)} = \epsilon_0 \hat{n} \left[\chi_{\perp\perp\perp}^{(2)} \mathbf{E}_{1\hat{n}} \mathbf{E}_{2\hat{n}} + \chi_{\perp\parallel\parallel}^{(2)} \left(\mathbf{E}_{1\hat{i}_1} \mathbf{E}_{2\hat{i}_1} + \mathbf{E}_{1\hat{i}_2} \mathbf{E}_{2\hat{i}_2} \right) \right] \\ + \hat{i}_1 \chi_{\parallel\perp\parallel}^{(2)} \mathbf{E}_{1\hat{n}} \mathbf{E}_{2\hat{i}_1} + \hat{i}_2 \chi_{\parallel\perp\parallel}^{(2)} \mathbf{E}_{1\hat{n}} \mathbf{E}_{2\hat{i}_2}, \end{aligned} \quad (2)$$

where \perp and \parallel refer to the orthogonal and tangential components to the nanoparticle surface. $(\hat{i}_1, \hat{i}_2, \hat{n})$ is a system of three orthogonal vectors, locally defined on the particle surface. The contributions of tangential and normal components of the surface nonlinear polarization are taken into account by the nonlinear surface electric and magnetic current sources:

$$\mathbf{J}_0^{(\nu)} = -i\nu \mathbf{P}_t^{(\nu)}, \quad (3)$$

$$\mathbf{M}_0^{(\nu)} = \frac{1}{\epsilon'} \hat{n} \times \nabla_S P_n^{(\nu)}, \quad (4)$$

where $\mathbf{P}_t^{(\nu)}$ and $P_n^{(\nu)}$ are the tangential and normal components of $\mathbf{P}^{(\nu)}$. The Boundary-Element Method is applied to solve the driven wave equation by invoking Love's Equivalence Principle. The domain of the electromagnetic field is divided into the interior of the metal domain, V_i , the exterior medium, V_e , and the interface, S . The object is illuminated by the plane-wave source, \mathbf{E}^{inc} . The equivalent currents, $\mathbf{J}_e^{(\nu)}, \mathbf{M}_e^{(\nu)}$, positioned on the external page, S^+ produce the scattered field in the region V_e , and a null field in the region V_i . The equivalent currents, $\mathbf{J}_i^{(\nu)}, \mathbf{M}_i^{(\nu)}$ defined on the internal side, S^- , produce the total field in the region V_i , and a null field in the region V_e .

$$\left. \begin{aligned} \mathbf{r} \in V_e, \mathbf{E}_\ell^{(\nu)}(\mathbf{r}) \\ \mathbf{r} \notin V_e, 0 \end{aligned} \right\} = \left. \begin{aligned} i\nu\mu_\ell \int_S \overline{\mathbf{G}}^{(\nu)}(\mathbf{r}, \mathbf{r}') \cdot \mathbf{J}_\ell^{(\nu)}(\mathbf{r}') d\mathbf{r}' \\ - \int_S \nabla \times \overline{\mathbf{G}}^{(\nu)}(\mathbf{r}, \mathbf{r}') \cdot \mathbf{M}_\ell^{(\nu)}(\mathbf{r}') d\mathbf{r}' \end{aligned} \right\} \quad (5)$$

where $\overline{\mathbf{G}}^{(\nu)}(\mathbf{r}, \mathbf{r}') = [\bar{\mathbf{I}} + k^{(\nu)-2} \nabla \nabla] \exp[ik^{(\nu)} R] / 4\pi R$ is the dyadic Green's function at frequency ν . Here,

$R = |\mathbf{r} - \mathbf{r}'|$. $\ell = e, i$ denote the exterior and interior regions of the object, respectively. The magnetic field has a similar representation. The equivalent currents satisfy

$$\mathbf{J}_i^{(\nu)} + \mathbf{J}_e^{(\nu)} = \mathbf{J}_0^{(\nu)}, \quad (6)$$

$$\mathbf{M}_i^{(\nu)} + \mathbf{M}_e^{(\nu)} = \mathbf{M}_0^{(\nu)}. \quad (7)$$

The surfaces of the nanostructures are discretized with a triangular mesh. The equivalent currents are expanded with Rao-Wilton-Glisson (RWG) basis functions [19]. A matrix system is then constructed by exploiting the Galerkin testing procedure. A modified Poggio-Miller-Chang-Harrington-Wu-Tsai (PMCHWT) formulation [20] is used to ensure accurate solutions, even at resonant conditions. The PMCHWT matrix equation can be written as

$$\bar{\mathbf{C}}^{(\nu)} \cdot \mathbf{X}^{(\nu)} = \mathbf{Y}^{(\nu)}. \quad (8)$$

The impedance matrix, $\bar{\mathbf{C}}^{(\nu)}$, is

$$\bar{\mathbf{C}}^{(\nu)} = \begin{bmatrix} \mathcal{L}_e^{(\nu)} & \mathcal{K}_e^{(\nu)} & -\mathcal{L}_i^{(\nu)} & -\mathcal{K}_i^{(\nu)} \\ -\mathcal{K}_e^{(\nu)} & \eta_e^{-2} \mathcal{L}_e^{(\nu)} & \mathcal{K}_i^{(\nu)} & -\eta_i^{-2} \mathcal{L}_i^{(\nu)} \\ \mathcal{I} & 0 & \mathcal{I} & 0 \\ 0 & \mathcal{I} & 0 & \mathcal{I} \end{bmatrix},$$

where $\mathcal{L}_\ell^{(\nu)} = i\nu\mu_\ell \bar{\mathbf{G}}^{(\nu)}$, and $\mathcal{K}_\ell^{(\nu)}$ is the principal value part of the $\mathcal{K}_\ell^{(\nu)}$ operator with $\mathcal{K}_\ell^{(\nu)} = -\nabla \times \bar{\mathbf{G}}^{(\nu)}$. $\eta_\ell = \sqrt{\mu_\ell / \varepsilon_\ell}$ with $\ell = e, i$. The vector of unknowns $\mathbf{X}^{(\nu)}$ and the excitation $\mathbf{Y}^{(\nu)}$ are

$$\mathbf{X}^{(\nu)} = \begin{bmatrix} \mathbf{J}_e^{(\nu)} \\ \mathbf{M}_e^{(\nu)} \\ \mathbf{J}_i^{(\nu)} \\ \mathbf{M}_i^{(\nu)} \end{bmatrix},$$

$$\mathbf{Y}^{(\nu)} = \begin{bmatrix} \frac{1}{2} \hat{\mathbf{n}} \times \mathbf{M}_0^{(\nu)} \\ -\frac{1}{2} \hat{\mathbf{n}} \times \mathbf{J}_0^{(\nu)} \\ \mathbf{J}_0^{(\nu)} \\ \mathbf{M}_0^{(\nu)} \end{bmatrix}.$$

Equation (8) can be used to solve for the fundamental fields as well, by setting $\nu = \omega_\alpha$, with $\alpha = 1, 2$ for frequencies ω_1 and ω_2 , respectively. The driven source is now the incident excitation

$$\mathbf{J}_0^{(\omega_\alpha)} = \hat{\mathbf{n}} \times \mathbf{H}^{(\omega_\alpha, inc)}, \quad (9)$$

$$\mathbf{M}_0^{(\omega_\alpha)} = -\hat{\mathbf{n}} \times \mathbf{E}^{(\omega_\alpha, inc)}. \quad (10)$$

The Boundary-Element Method formulation can efficiently model the nonlinear scattering from arbitrarily shaped particles since it only requires surface discretization. In addition, measured material parameters can directly be used. In this work, $\chi_{\perp\perp\perp}^{(2)} = 1.59 \times 10^{-18} \text{ m}^2/\text{V}$, and only the normal component, $\chi_{\perp\perp\perp}^{(2)}$, of the surface susceptibility tensor was considered, since it is the dominant term of the surface response of metallic nanoparticles. Note that other components are theoretically allowed, but they weakly contribute to the total second-harmonic response.

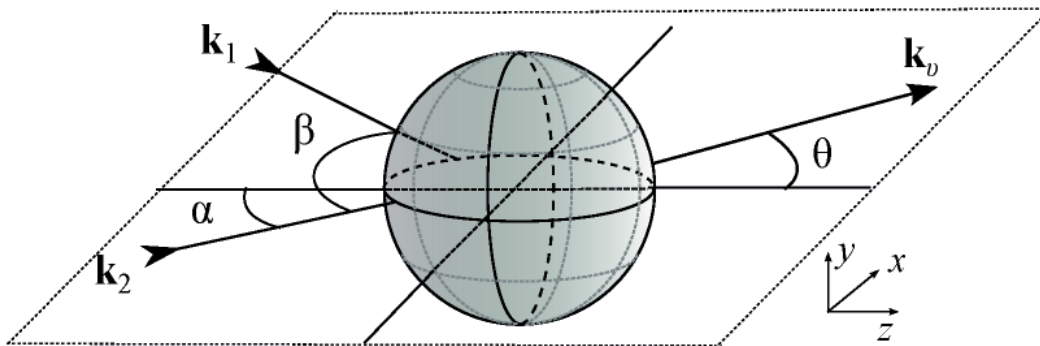


Figure 1. An overview of the relevant parameters in the model: The sum-frequency and source waves had wave vectors \mathbf{k}_ν , \mathbf{k}_1 , and \mathbf{k}_2 , in order of decreasing frequency. The angle between the propagation direction of the lowest-frequency wave and the positive z axis was α ; the opening angle between source waves was β . The sum-frequency scattering pattern was parameterized using the scattering angle θ [22].

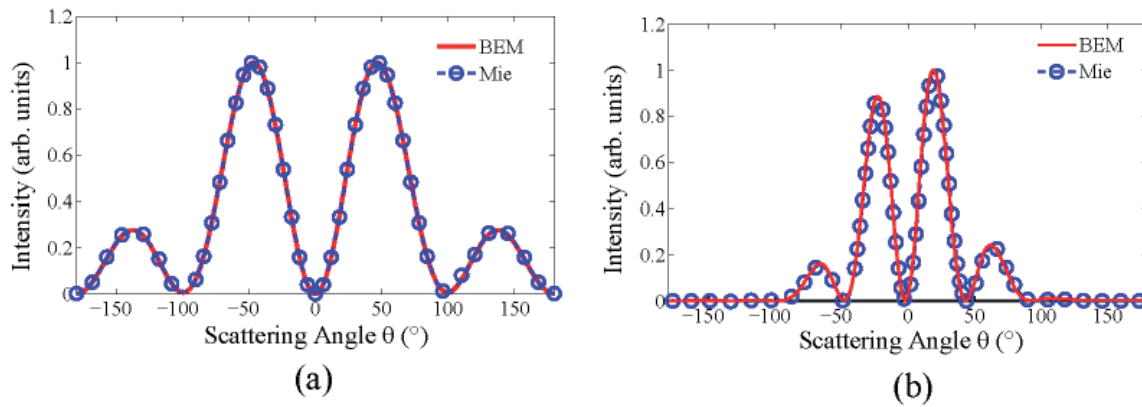


Figure 2. Comparisons of sum-frequency and second-harmonic scattering patterns with the nonlinear Mie solutions: (a) The sum-frequency scattering pattern. The simulation parameters were $R = 500$ nm ; $\lambda_1 = 800$ nm and $\lambda_2 = 3447$ nm ; $\beta = 15^\circ$. (b) The second-harmonic scattering pattern. The simulation parameters were $R = 50$ nm ; $\lambda_1 = 520$ nm.

3. Numerical Results

3.1 Verification of the Algorithm

We first validated the Boundary-Element Method algorithm by comparing the sum-frequency (SF) and second-harmonic (SH) scattering patterns of spherical nanoparticles with the nonlinear Mie solutions [21, 22]. For sum-frequency generation, two incident plane waves propagating at different angles with different frequencies were superposed, as shown in Figure 1. The polarization angles (defined as the angle between $-\hat{\theta}$ and \mathbf{E}) were set to zero for both incident waves. Figure 2a shows the comparison of the sum-frequency scattering patterns. Very good agreement was observed. Here, the radius of the sphere was $R = 500$ nm. The wavelengths of the

incident waves were $\lambda_1 = 800$ nm and $\lambda_2 = 3447$ nm, respectively. The opening angle between the source waves was $\beta = 15^\circ$, and the index of refraction was set to unity for all wavelengths. The asymmetry in the sum-frequency scattering pattern was due to the nonzero opening angle between source beams. For second-harmonic generation, a single electromagnetic field was taken as the source. A gold sphere with a radius of $R = 50$ nm was excited by a plane wave propagating along the positive direction of the z axis, and linearly polarized along x . The exciting wavelength, $\lambda = 520$ nm, corresponded to the plasmon resonance of the gold spherical particle. The dielectric constant for gold was taken from experimental data [23]. We could see that the second-harmonic scattering pattern calculated by the Boundary-Element Method agreed well with the nonlinear Mie-theory result.

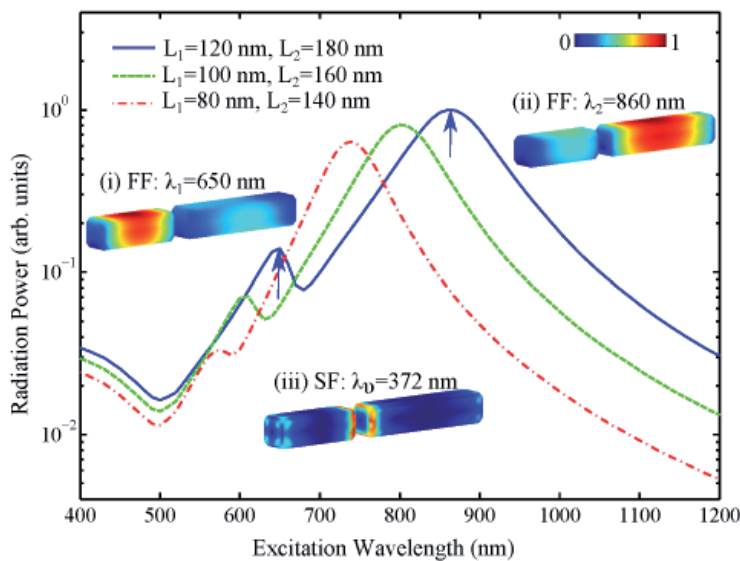


Figure 3. The radiation power of the multi-resonant nanoantenna as a function of the incident wavelength with different arm lengths. The arrows denote the resonant peaks of the multi-resonant nanoantenna with arm lengths $L_1 = 120$ nm and $L_2 = 180$ nm. The inset shows the distribution of fundamental and sum-frequency equivalent electric currents on the surface of the multi-resonant nanoantenna.

3.2 Sum-Frequency Generation from Multi-Resonant Nanoantenna

The multi-resonant nanoantenna consisted of two gold arms of different lengths, L_1 and L_2 ($L_1 < L_2$). The separation between the two arms was fixed at 20 nm. The width and height of the antenna arms were 40 nm. The lengths of the metal arms corresponded to two resonant frequencies, ω_1 and ω_2 , respectively. Figure 3 shows the radiation power as a function of the incident wavelength with different arm lengths. Due to the asymmetry of the antenna design, two resonant peaks were observed, and they were red-shifted with the increase in the arm lengths. The insets in Figure 3 show the distribution of fundamental frequency and sum-frequency equivalent electric currents on the surface of the multi-resonant nanoantenna. The resonant peak at $\lambda_1 = 650$ nm corresponded to the half-wave resonance of the short arm, as presented in inset (i). Similarly, the resonant peak at $\lambda_2 = 860$ nm corresponded to the long arm's resonance, as presented in inset (ii). The nonlinear equivalent currents at the sum-frequency with $\lambda_\nu = 372$ nm were concentrated near the gap and corners of the arms.

3.3 Second-Harmonic Generation from Particle-in-Cavity Nanoantenna

The configuration of the investigated particle-in-cavity nanoantenna is depicted in Figure 4a. A gold nanosphere with a diameter of $D = 40$ nm was located inside a gold rounded-edge nanocup cavity, separated by a small gap of $g = 5$ nm. The nanocup cavity used was a truncated hemispherical nanoshell with external and inner radii of $R_1 = 120$ nm and $R_2 = 160$ nm, respectively. Depending on the angle between the center of the nanosphere and the symmetry axis of the nanocup, the nanoantenna possessed symmetric ($\beta = 0^\circ$) or asymmetric ($\beta = 30^\circ$) geometry. The particle-in-cavity nanoantenna was illuminated by a y -polarized plane wave at normal incidence from the top side. The linear and nonlinear responses of the particle-in-cavity nanoantenna were numerically simulated by the Boundary-Element Method.

Placing a metallic nanoparticle inside a cavity produced extremely strong field enhancements at the particle-cavity gap when one of the cavity modes was

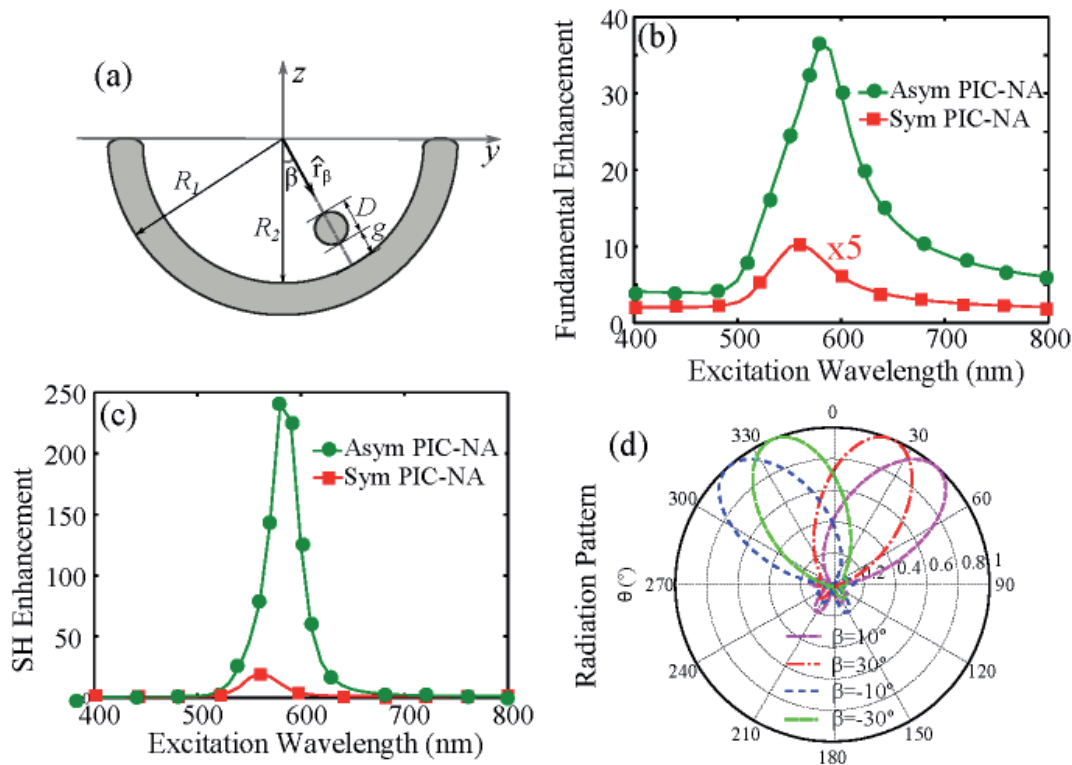


Figure 4. (a) A schematic drawing of the particle-in-cavity nanoantenna (yoz plane). A nanosphere (diameter D) was inside a nanocup cavity (external and inner radii being R_1 and R_2) separated by a gap, g . The angle between the center of the nanosphere and the symmetry axis of the nanocup was β . (b) The fundamental and (c) second-harmonic enhancement spectra of the symmetric and asymmetric particle-in-cavity nanoantenna. (d) The steering of the main beam of the radiation pattern (yoz plane) at the resonant wavelength by manipulating the position of the particle.

resonant with the cavity-dressed nanoparticle mode. The fundamental field enhancement was investigated at a fixed point (the center of the gap). The enhancement factor is defined as the ratio of the magnitude of the scattered field at the center of the gap to the magnitude of the incident field. Figure 4b shows the calculated fundamental field-enhancement spectra of the particle-in-cavity nanoantenna. Enhancement factors of roughly 2 at $\lambda = 560$ nm and 37 at $\lambda = 580$ nm were found for the symmetric and asymmetric cases, respectively. Because the second-harmonic field increased as the square of the fundamental field, a strong near-field at the fundamental frequency was particularly important for efficient second-harmonic generation enhancement.

The second-harmonic enhancement factor is defined as the ratio of the second-harmonic intensity of the particle-in-cavity nanoantenna to the summation of the second-harmonic intensities of the single nanosphere and nanocup. Figure 4c shows the second-harmonic enhancement factor. The correlation between the fundamental field-enhancement spectra (Figure 4b) and the second-harmonic intensity spectra (Figure 4c) demonstrated that the second-harmonic generation from the particle-in-cavity nanoantenna was boosted by the enhanced field intensity arising from the gap plasmonic mode. The radiation pattern of the particle-in-cavity nanoantenna is shown in Figure 4d. Unidirectional radiation was observed. This important feature further enhanced the second-harmonic generation in the far field, and facilitated the detection of the generated second-harmonic waves. Moreover, beam-steering feature was achieved by changing the position of the nanosphere.

4. Conclusion

In summary, the Boundary-Element Method was developed for modeling surface nonlinear scattering from plasmonic nonlinear nanoantennas. The method was validated by comparing far-field sum-frequency and second-harmonic scattering patterns with Mie theory solutions. The sum-frequency generation from the multi-resonant nanoantenna, where two incident frequencies corresponded to the fundamental resonances of the two arms, was analyzed by the developed method. The second-harmonic generation from the particle-in-cavity nanoantenna was also modeled by the developed method. Unidirectional radiation of asymmetric particle-in-cavity nanoantenna was realized, and the radiation direction could be controlled by the position of the nanoparticle. The directional beam steering offered by the proposed particle-in-cavity nanoantenna has promising applications, such as nonlinear sensing, spectroscopy, and frequency generation.

5. Acknowledgement

This work was supported in part by the Research Grants Council of Hong Kong (GRF 17207114 and

GRF 17210815), NSFC 61271158, Hong Kong UGC AoE/P-04/08, and by the US NSF 1218552 and NSF 1609195.

6. References

1. M. Kauranen and A. V. Zayats, "Nonlinear Plasmonics," *Nature Photonics*, **6**, 2012, pp. 737-748.
2. S. A. Maier, *Plasmonics: Fundamentals and Applications*, New York, Springer, 2007.
3. Y. R. Shen, *The Principle of Nonlinear Optics*, New York, John Wiley & Sons, Inc., 1984.
4. J. E. Sipe, V. C. Y. So, M. Fukui, and G. I. Stegeman, "Analysis of Second-Harmonic Generation at Metal Surfaces," *Physical Review B*, **21**, 1980, pp. 4389-4395.
5. C. Ciraci, E. Poutrina, M. Scalora, and D. R. Smith, "Origin of Second-Harmonic Generation Enhancement in Optical Split-Ring Resonators," *Physical Review B*, **85**, 2012, p. 201403.
6. J. Butet, K. Thyagarajan, and O. J. F. Martin, "Ultrasensitive Optical Shape Characterization of Gold Nanoantennas Using Second Harmonic Generation," *Nano Letters*, **13**, 2013, pp. 1787-1792.
7. V. K. Valev, "Characterization of Nanostructured Plasmonic Surfaces with Second Harmonic Generation," *Langmuir*, **28**, 2012, pp. 15454-15471.
8. J. Butet, I. Russier-Antoine, C. Jonin, N. Lascoux, E. Benichou, and P.-F. Brevet, "Sensing with Multipolar Second Harmonic Generation from Spherical Metallic Nanoparticles," *Nano Letters*, **12**, 2012, pp. 1697-1701.
9. G. Bautista, M. J. Huttunen, J. Makitalo, J. M. Kontio, J. Simonen, and M. Kauranen, "Second-Harmonic Generation Imaging of Metal Nano-Objects with Cylindrical Vector Beams," *Nano Letters*, **12**, 2012, pp. 3207-3212.
10. H. Harutyunyan, S. Palomba, J. Renger, R. Quidant, and L. Novotny, "Nonlinear Dark-Field Microscopy," *Nano Letters*, **10**, December 2010, pp. 5076-5079.
11. G. Sartorello, N. Olivier, J. Zhang, W. Yue, D. J. Gosztola, G. P. Wiederrecht, G. Wurtz, and A. V. Zayats, "Ultrafast Optical Modulation of Second- and Third-Harmonic Generation from Cut-Disk-Based Metasurfaces" *ACS Photonics*, **3**, 2016, pp. 1517-1522.
12. G. F. Walsh and L. Dal Negro, "Enhanced Second Harmonic Generation by Photonic-Plasmonic Fano-Type Coupling in Nanoplasmonic Arrays," *Nano Letters*, **13**, 2013, pp. 3111-3117.

13. K. Thyagarajan, J. Butet, and O. J. F. Martin, "Augmenting Second Harmonic Generation Using Fano Resonances in Plasmonic Systems," *Nano Letters*, **13**, 2013, pp. 1847-1851.
14. K. Thyagarajan, S. Rivier, A. Lovera, and O. J. F. Martin, "Enhanced Second-Harmonic Generation from Double Resonant Plasmonic Antennae," *Optics Express*, **20**, June 2012, pp. 12860-12865.
15. X. Y. Z. Xiong, L. J. Jiang, W. E. I. Sha, Y. H. Lo, and W. C. Chew, "Compact Nonlinear Yagi-Uda Nanoantennas," *Scientific Reports*, **6**, January 2016, p. 18872.
16. X. Y. Z. Xiong, L. J. Jiang, W. E. I. Sha, Y. H. Lo, M. Fang, W. C. Chew, and C. H. Choy, "Strongly Enhanced and Directionally Tunable Second-Harmonic Radiation by a Plasmonic Particle-in-Cavity Nanoantenna," *Physical Review A*, **94**, November 2016, p. 053825.
17. R. Czaplicki, J. Makitalo, R. Siikanen, H. Husu, J. Lehtolahti, M. Kuittinen, and M. Kauranen, "Second-Harmonic Generation from Metal Nanoparticles: Resonance Enhancement Versus Particle Geometry," *Nano Letters*, **15**, 2015, pp. 530-534.
18. R. W. Boyd, *Nonlinear Optics*, New York, Academic Press, 1992.
19. S. M. Rao, G. R. Wilton, and A. W. Glisson, "Electromagnetic Scattering by Surfaces of Arbitrary Shape," *IEEE Transactions on Antennas and Propagation*, **AP-30**, 3, May 1982, pp. 409-418.
20. L. N. Medgyesi-Mitschang, J. M. Putnam, and M. B. Gedera, "Generalized Method of Moments for Three-Dimensional Penetrable Scatterers," *Journal of the Optical Society of America A*, **11**, April 1994, pp. 1383-1398.
21. J. I. Dadap, J. Shan, and T. F. Heinz, "Theory of Optical Second-Harmonic Generation from a Sphere of Centrosymmetric Material: Small Particle Limit," *Journal of the Optical Society of America B*, **21**, 2004, pp. 1328-1347.
22. A. G. F. de Beer and S. Roke, "Nonlinear Mie Theory for Second-Harmonic and Sum-Frequency Scattering," *Physical Review B*, **79**, 2009, p. 155420.
23. P. B. Johnson and R. W. Christy, "Optical Constants of Noble Metals," *Physical Review B*, **6**, 1972, pp. 4370-4379.